

# RESEARCH ON MICROSEISMIC EVENT LOCALIZATION BASED ON CONVOLUTIONAL NEURAL NETWORK

ZHANG YAN<sup>a</sup>, WEI ZI-XIN<sup>a</sup>, CUI LIN-QI<sup>b</sup>, DONG HONG-LI<sup>c,d</sup>

<sup>a</sup>*School of Computer and Information Technology, Northeast Petroleum University, Da Qing, Heilongjiang, 163318, China;*

<sup>b</sup>*School of Medical Information Engineering, Heilongjiang University of Chinese Medicine, Ha Erbin, Heilongjiang, 150006, China;*

<sup>c</sup>*Artificial Intelligence Energy Research Institute, Northeast Petroleum University, Da Qing, Heilongjiang, 163318, China;*

<sup>d</sup>*Key Laboratory of Networking and Intelligent Control of Heilongjiang Province, Da Qing, Heilongjiang, 163000, China;*

*\*Corresponding author: ZHANG Yan*

(Received February 24, 2024; revised version accepted August 06, 2024)

## ABSTRACT

Microseismic monitoring technology is one of the most critical technologies used in hydraulic fracturing. The positioning accuracy and efficiency of microseismic sources significantly influence the performance of this technology. This study proposes a microseismic source localization method based on convolutional neural networks that transforms the inversion problem of solving source positions into a mapping problem of constructing the probability distribution of source positions from microseismic data. First, when constructing the dataset, factors affecting the accuracy of source positioning are considered, and velocity model errors and noise interference are introduced for data augmentation. Second, a convolutional neural network model, termed MEL-Net, is developed, which is based on the classic U-Net network architecture and integrates an attention mechanism and a spatial hole multiscale pooling module to improve feature extraction. Furthermore, no feature concatenation operation is performed in shallow-level encoding and decoding to reduce the interference of irrelevant information with positioning tasks. Finally, the applicability of the method is verified using a simple layered velocity model and a complex Marmousi model. The results show that MEL-Net can achieve accurate source location predictions. In the measurement process, it is more robust than U-Net. Compared with the traditional reverse-time positioning algorithm, it is insensitive to factors such as speed model errors and noise interference. It significantly improves the positioning speed while providing accurate microseismic source location predictions.

**KEY WORDS:** Microseismic; Event location; U-Net; Attentional mechanism; Atrous spatial pyramid pooling

## INTRODUCTION

Microseismic source positioning is a part of the microseismic monitoring process. Information collected using a geophone is analyzed and processed to obtain the spatial form of the formation of groundwater hydraulic fracturing cracks, which is helpful for fracturing engineers to adjust the injection optimization strategy in time to provide data reference (Wang Jiachen, 2023). The reverse-time positioning algorithm does not need to pick up the first arrival when solving the source position, which can eliminate the error caused by the linearization of the nonlinear problem (Cheng Jiulong, 2018). It is widely used in the location task of microseismic events (Xu Li-sheng, 2013; Ge Oixin, 2019; Li F, 2019; Cheng Qian, 2022). To obtain more robust and accurate positioning results, domestic and foreign scholars have improved the reverse-time positioning algorithm. For example, some scholars have combined the principles of reverse-time focusing and interference imaging (Sava O M, 2011; Wang H, 2013; Guo X B, 2018). The resolution of the source location is improved while the background noise is suppressed. Another improvement idea is to optimize the imaging operator to improve positioning efficiency and imaging quality (Yuan J, 2020; Tang Jie, 2021; Zhang Lingli, 2021; Tian Xiao, 2020). In addition, Li Meng (Li Meng, 2019) proposed a multiscale reverse-time imaging technique that decomposes the original waveform and applies the reverse-time positioning algorithm to each time-frequency domain waveform to suppress imaging artifacts. Feng Q (Feng Q, 2021) proposed an inverse double-difference time imaging method to reduce the impact of velocity model errors. The advantage of the reverse-time positioning algorithm is that it does not need to perform accurate first arrival-picking tasks; however, it is still affected by many factors in the application process. The existing problem is the improvement of positioning accuracy and the requirement of real-time positioning for algorithm efficiency. Therefore, it is urgent to combine new technologies and methods to further optimize the positioning method to achieve broader application.

With the development of artificial intelligence, the emergence of deep learning has changed the analysis and processing of problems. Source location algorithms based on deep learning transform complex inversion problems of conventional methods into mapping relationships between seismic gathers and source locations. Based on the realization mechanism, it can be divided into two types, the first of which is to identify and locate the microseismic data. Huang L Q (Huang L Q, 2018) developed a convolutional neural network (CNN) model. The inputs of the network are power and phase spectra calculated from the travel time of microseismic events. The output is the reciprocal time difference in the microseismic events, from which the source location is determined. Saad O M (Saad O M, 2021) developed an unsupervised learning method based on a variational autoencoder and an attention mechanism module to identify microseismic signals in strong noise and used the processed data for reverse-time continuation imaging. Wang H (Wang H, 2021) developed two CNNs. After a microseismic event was detected by a previous network,

the latter network was used to determine the source location of the event and its amplitude, frequency, and other related parameters. The main function of the neural network in this type of method is to first complete the identification of microseismic signals and then locate the operation through the information extracted from the network output. Feng Qiang (Feng Qiang, 2023) built a joint positioning model of convolutional noise reduction self-encoder and SoftMax regression classifier, which transformed microseismic positioning into a supervised classification problem while suppressing random noise, and output multiple classification labels of pending microseismic events in a classification way, thus determining the source location.

Another positioning idea is to use neural networks to construct a mapping from a seismic waveform directly to the source location coordinates. For example, Perol T (Perol T, 2018) regarded source location as a classification task and proposed a new network model, ConvNetQuake, that uses three-component waveform records as input to predict whether the waveform corresponds to seismic noise or seismic events in geographic clusters. Zhang Xiong (Zhang Xiong, 2020) developed a fully convolutional network (FCN) model to predict the three-dimensional probability distribution of the source location from three-component waveforms recorded by multiple stations. The research object of the above two methods is the seismic activity of Oklahoma in the United States, which does not meet the positioning accuracy required for microseismic monitoring but fundamentally changes the limitations of conventional positioning methods. For the automatic location of microseismic events, Wang Chen-Long. (Wang Chen-Long, 2013) regarded the location task as multitask learning and defined the source coordinates ( $X_0$ ,  $Y_0$ ,  $Z_0$ ) as three tasks X, Y, and Z for network output. The experimental results show that the proposed algorithm can accurately predict the location of microseismic events. Ma K (Ma K, 2022) modified the loss function based on the full convolutional neural network, and constructed a dataset based on the microseismic events near the Zhangjiakou underground power plant in southwest China. The experimental results show that the method improves the positioning efficiency to a certain extent. Wamriew D (Wamriew D, 2022) inversed the velocity model while locating the microseismic source based on the AlexNet network. Zhang Y (Zhang Y, 2024) made further improvements in velocity model inversion; Vinard N A (Vinard N A, 2022) combined CNNs with transfer learning ideas, used synthetic datasets for data augmentation, and used smaller datasets to update network weights after training based on the U-Net network. The experimental results show that the model using the augmented dataset combined with the idea of transfer learning exhibits significant performance improvement. The advantage of this method is the formation of an “end-to-end” network architecture. Once the network is trained, the corresponding source location can be directly determined by inputting waveform information.

Deep learning-based methods are based on the powerful automatic feature extraction ability of deep learning, and feature learning is performed using all

information from microseismic signals. The positioning results are unaffected by prior knowledge, which mitigates the trade-off between the positioning accuracy and operation efficiency of the traditional algorithm. However, there are still problems. First, the signal-to-noise ratio (SNR) of microseismic signals is low. When the current algorithm uses the gathered data as network input, the influence of noise is typically ignored in the process of mapping to the source location. Second, when solving the problem of minimizing the error of approaching the source position through the characteristics of microseismic data, the limited support characteristics make the model have high multiple solutions, which affects the positioning effect.

Based on this, this study proposes a microseismic source location method based on a CNN, called microseismic event location-net (MEL-Net). The network is based on the U-Net model and combines an attention mechanism module and a spatial hole multiscale module to perform effective feature extraction from microseismic data, reduce noise interference (Zhang Y, 2023), and improve the accuracy of support features so that the neural network can fully learn the mapping relationship between the waveform characteristics of microseismic events and the source location. In this study, the basic principle and related network model of positioning tasks are introduced. Then, a dataset is prepared and trained. Single-source and multisource positioning experiments are conducted using a simple velocity model, and the rationality of the proposed method is verified by ablation experiments.

Second, the Marmousi model is used to test the positioning effect of the network when the SNR is low and the velocity model has errors; the robustness of the model is evaluated. Finally, the advanced nature of the proposed method is proved by comparing it with the traditional reverse-time positioning algorithm.

## THEORY

### **Influencing factors of positioning accuracy**

In the underground rock medium, rock fracture causes microseism, and energy is transmitted to the detector in the form of a seismic wave. Source location mainly uses information contained in collected microseismic data, such as travel time, first arrival time, and three-component waveform information about shear or longitudinal waves, to obtain spatial location information about the source of an event. A schematic of the location process is shown in Fig.1. Accurate source location is the basis of all quantitative analyses. Factors affecting positioning accuracy can be roughly divided into the following three aspects:

- 1) **Observational conditions.** Microseismic data obtained during microseismic monitoring are limited by the observation conditions. The use of a geophone array can improve the certainty of positioning to a certain extent.

In practical applications, the influence of the detector array on the positioning results mainly lies in whether the rupture event area is completely included and the target layer is well covered. When more seismic traces with only noise and no microseismic events are recorded in the geophone, the calculated positioning results have significant errors. Under the same conditions, the greater the geometric coverage of the detector to the target monitoring area, the higher the positioning accuracy.

2) Noise interference. The influence of noise in the propagation process of microseismic signals cannot be ignored, including regular coherent noise and background random noise. Because the microseismic energy is typically weak and the amplitude is small, noise interference makes the microseismic waveform complex. The effective waveform in the trace data is mixed with the noise waveform, making the characteristics of the effective signal impossible to distinguish.

3) Accuracy of velocity model. The accuracy of velocity models is directly related to positioning accuracy. However, in practical applications, accurately modeling the actual wave velocity of seismic waves propagating in rock media is difficult. Typically, simplified velocity models are used to approximate the true wave velocity, resulting in significant differences between the calculated and true wave velocities and positioning errors.

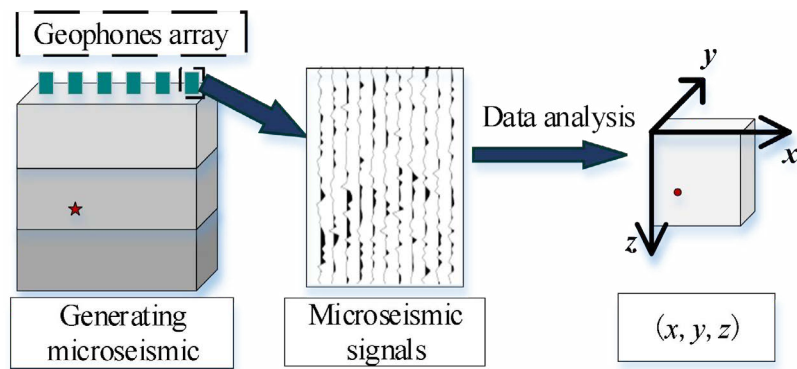


**Fig. 1** Schematic diagram of microseismic source positioning

In summary, source positioning accuracy is affected by factors such as the observation system, noise, and velocity model errors. Positioning algorithms based on deep learning should consider signal characteristics during the development and design of reasonable and efficient network models for applications.

## U-Net

U-Net was first proposed by Ronneberger O (Ronneberger O 2015) and is widely used in medical segmentation tasks. It is a variant of FCNs (Long J,

2015). The network contains an encoding structure for obtaining input data features and a decoding structure for restoring spatial dimensions and details. The network model structure is shown in Fig.2.

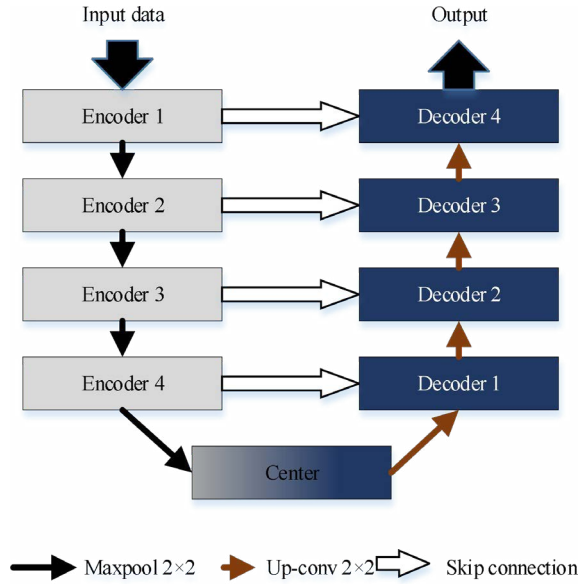


**Fig.2** Convolutional Neural Network U-Net Network structure

In the U-Net network structure, the encoding and decoding networks are symmetrical. In the encoding network, the resolution of the feature map is continuously reduced, and detailed information such as the contour and texture of the input image and additional abstract semantic information are obtained to achieve multiscale information extraction. The multilevel pooling operation makes the network insensitive to the disturbance of input information and reduces the influence of noise. Unlike FCNs, U-Net uses skip connections for cross-layer splicing and a skip concatenation method for cross-layer stitching. During the upsampling process, the feature map dimension does not change; however, it also contains additional detailed features, retaining additional position information, which gives it an advantage in positioning tasks.

Currently, the use of U-Net is no longer limited to the processing of medical images. It is also typically applied to the processing of microseismic signals to complete classification or regression tasks (Zhang Xiong, 2021; Vinard N A, 2021). In this study, the microseismic source location task is a regression task, and the U-Net network is used as the basic network architecture. Microseismic signals are used as input data, and the network output is the probability distribution image of the source location, forming an end-to-end network model.

### MEL-Net

To improve the positioning accuracy of the network, this study improves the U-Net network and proposes the MEL-Net network structure. The network

model structure is shown in Fig.3. The network model is a 6-layer encoder-decoder structure. The convolution layer uses a  $3 \times 3$  convolution kernel. ReLU is used as the activation function of the encoding and decoding networks. The batch normalization module is used in each layer of the network to normalize the output features of each layer to increase the stability of the training. In the last layer of the network, the Sigmoid activation function is used to map the output range to 0-1, which is used to represent the distribution probability of the source location. The main features of the network are as follows:

4) The task of the positioning model is to map time-domain information in microseismic data to the spatial-domain information of the probability distribution of the source location. There is a weak correspondence between the data in the element space. The detailed information extracted using a shallow convolution kernel, including noise, has a weak correlation with the positioning task. Therefore, the feature splicing operation is not performed on shallow encoding-decoding information when constructing the positioning model.

5) Based on the low SNR of the microseismic data, a spatial attention mechanism is used to assign different weights to different features in the seismic trace to highlight the effective waveform information and reduce the interference of background noise on the positioning task.

6) To solve the problems of the limited receptive field and insufficient extraction of high-level semantic information in the process of traditional convolution operation, the spatial hole multiscale pooling module is used to replace the original bridge module at the bottom of the encoder-decoder to improve the ability of the network to capture and learn features.

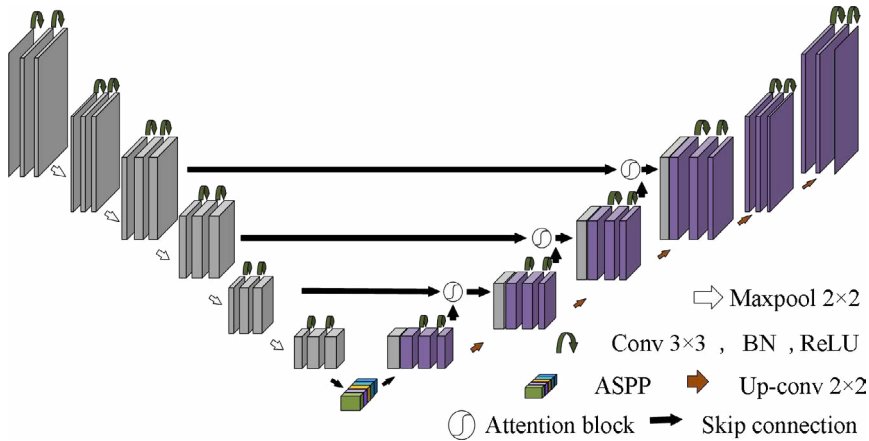


**Fig.3** Algorithm network model in this paper

### Attention mechanism

Starting from the idea of weight distribution and task focus, MEL-Net introduces an attention mechanism to avoid the interference of massive information and highlight key feature information. By endowing the neural

network with explicit attention ability to redistribute weights according to the contribution to key features, it reflects the correlation between the output prediction result graph and some specific position features of the input data.

In the process of microseismic source location, monitoring data are disturbed by noise, and the location task focuses on changes in the effective microseismic waveform. The introduction of an attention mechanism can integrate shallow coding and decoding information at the same level to suppress noise interference in the network model and realize accurate prediction of the source location. The process of task focus is reflected in the distribution of weight coefficients. The calculation formula for attention weight is shown in (1).

$$\begin{aligned} q_i^l &= \varepsilon_1(W_c^T c_i^l + W_g^T + b_1) \\ a_i^l &= \varepsilon_2(W_q^T q_i^l + b_2) \end{aligned} \quad (1)$$

where  $c^l$  denotes the encoder characteristic matrix;  $l$  denotes the corresponding decoder feature matrix;  $b_1$  and  $b_2$  denote the weight bias terms;  $W$  represents the transformation parameter matrix;  $\varepsilon_1$  denotes the operation through the ReLU activation function;  $\varepsilon_2$  denotes the operation after the Sigmoid function;  $l$  denotes the characteristic matrix obtained using the ReLU function;  $l$  denotes the final attention weight matrix. The working principle is shown in Fig.4.

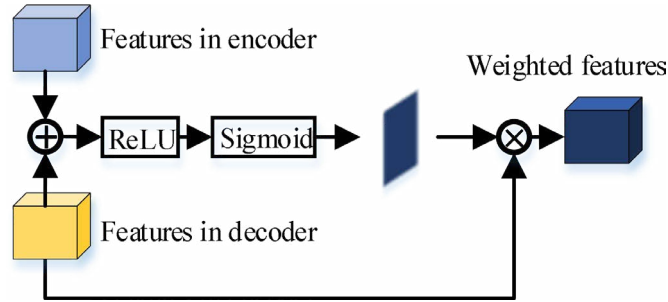


Fig.4 Principle of attention weight calculation

The feature map of the coding part is normalized by the ReLU activation function to obtain the attention weight. The feature in the decoder is multiplied by the weight to obtain the final output activation feature; that is, the weight represents the importance of information to realize the screening and focusing of key features.

### Space hole multi-scale pooling module

In the coding network, as the number of layers increases, the spatial dimension of the feature map gradually decreases, but the extracted features become more advanced and semantically richer. In the traditional U-Net network, the bridge module between encoding and decoding is simply upgraded after feature

splicing, which lacks the effective use of high-level features; thus, positioning accuracy cannot be guaranteed during the continuous upsampling process. Chen L C (Chen L C, 2018) proposed the atrous spatial pyramid pooling (ASPP) method. The ASPP module uses a series of dilated convolutional layers with different dilation rates to sample the target object and simultaneously obtain receptive fields of different scales. Using a dilated convolution with a size of

$k \times k$  and an expansion rate of  $d_r$ , the size  $k^{\square}$  of the ordinary convolution kernel equivalent to the receptive field is given by(2)

$$\tilde{k} = (k - 1) \cdot d_r + 1 \quad (2)$$

In this study, the algorithm uses the ASPP module instead of the original bridge module at the bottom of the U-Net network. After the feature map is extracted from the encoder using the ASPP module, it is provided to the decoder part of the network, which can retain important features in the high-level convolution to a great extent and provide multiscale and multilevel information for the subsequent upsampling operation. The expansion rates of the three parallel convolutional layers in this study are 6, 12, and 18, respectively. The schematic is shown in Fig.5. The global average pooling layer is used to obtain global feature information, and the  $1 \times 1$ -sized convolution layer fuses the obtained features and transmits them to the decoding network.

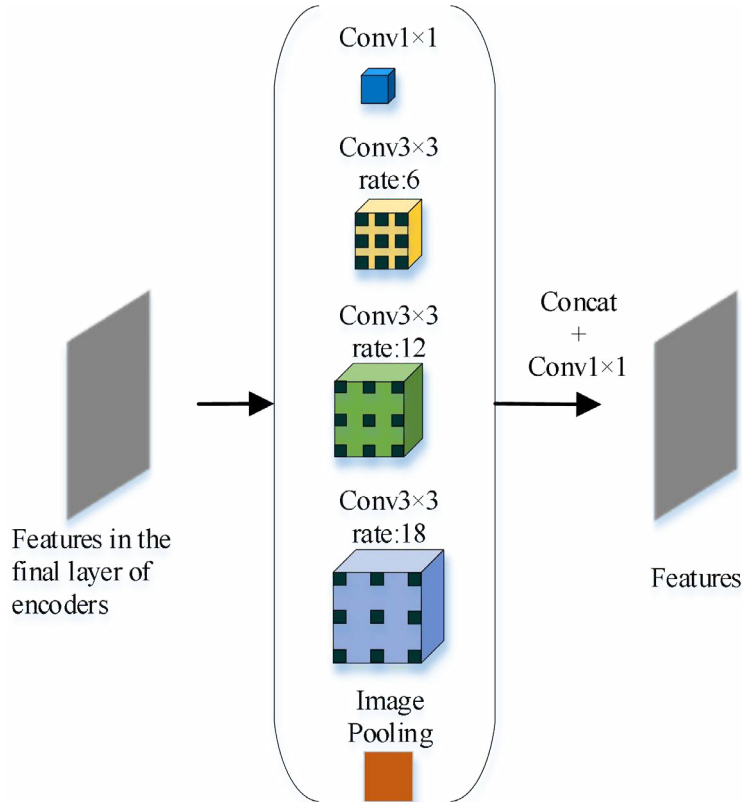


Fig.5 Schematic diagram of ASPP

## ALGORITHM AND IMPLAMENTATION

### Construction of training data and sample labels

The input of the network is the observation data collected using a geophone. If the microseismic data are directly introduced into the neural network for feature extraction, the feature dimension is adjusted by pooling operations, which reduces the training efficiency of the model. When the input feature has a small position change, the feature obtained after a series of pooling operations may remain unchanged, and the position information of the microseismic waveform is lost during the positioning task. For multichannel microseismic records, each signal is a continuous time function, and the microseismic data are preprocessed. In two-dimensional (2D) microseismic data, a certain proportion is sampled along the time direction, and the number of sampling points is consistent with the number of grid points in the  $z$  direction of the velocity model.

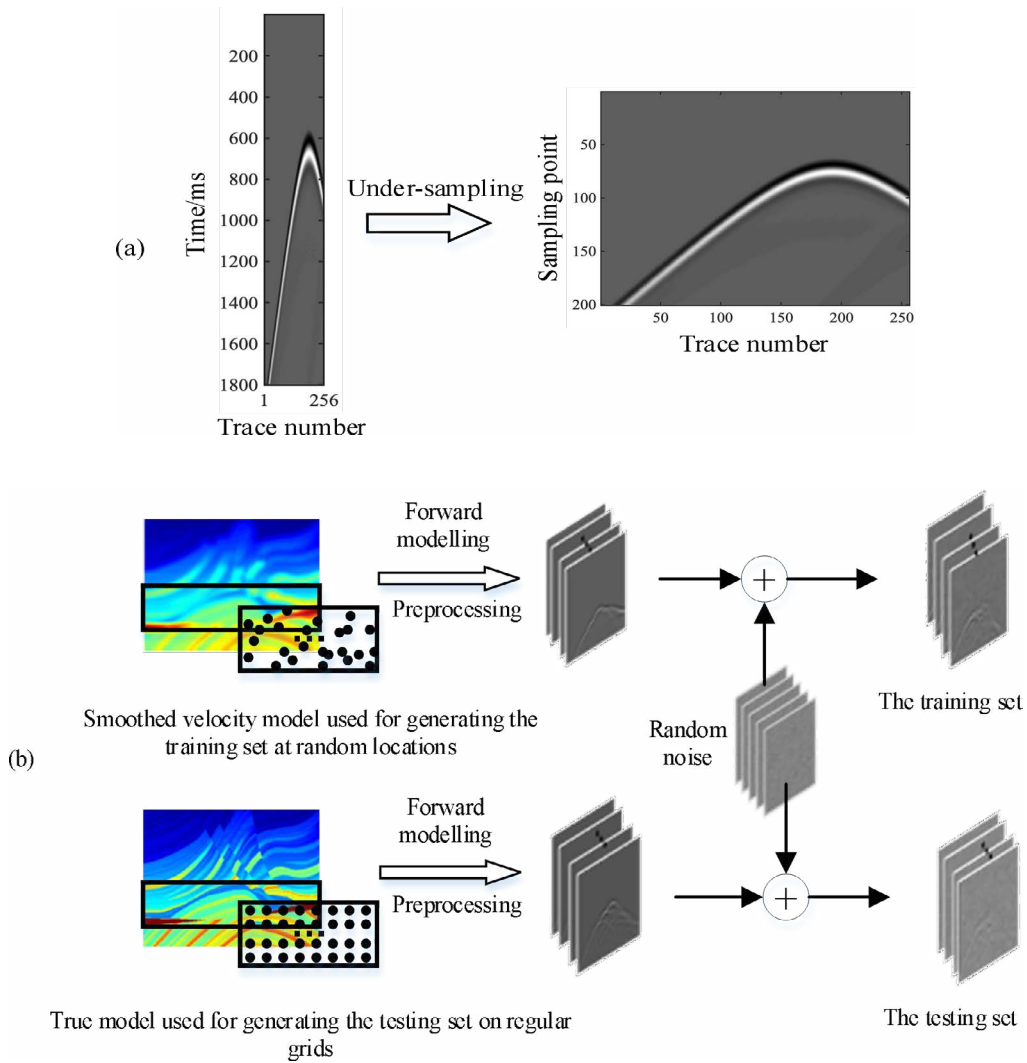
To obtain a more robust algorithm model, according to the influencing factors of source positioning accuracy, the velocity model error and noise interference are considered when constructing the microseismic dataset. Taking the Marmousi velocity model as an example, the smoothing operator with the size of  $4 \times 4$  and  $6 \times 6$  is used to smooth the  $x$  and  $z$  directions of the

original velocity model, respectively. The smoothed velocity model is used as the initial velocity model for numerical simulations. Gaussian noise with 20%–60% intensity is randomly added to the preprocessed microseismic data. The percentage of noise intensity is measured by the maximum amplitude in the microseismic waveform to obtain a sufficient input microseismic dataset. The dataset construction process is shown in Fig.6, where the black box represents the target monitoring area, and the black dots represent the position distribution of the source in the target area. When the training dataset is constructed, the source position is randomly distributed in the monitoring area. When constructing the test dataset, the source location is distributed according to the grid point rule.

The output label of the neural network is the probability distribution map of the source position. The label of each event is set to a 2D Gaussian distribution with a peak value of 1. The peak position is the source position corresponding to the microseismic event. The definition of the Gaussian distribution is as follows:

$$f(x, z) = \exp \left[ -\frac{(x - x_0)^2 + (z - z_0)^2}{d} \right] \quad (3)$$

Where  $(x_0, z_0)$  denotes the source position coordinate,  $d$  represents the variance of the Gaussian function



(a) Microseismic data before and after preprocessing (b) Production process of training and testing datasets

Fig. 6 Dataset production process.

The size of the monitoring area is represented by the number of grid points in the monitoring area, and each pixel value in the output map represents the probability value of the source at the corresponding grid position. After this operation, the input and output of the network have the same size, and the mapping relationship between the two is learned by MEL-Net.

### Network training process and parameter selection

Fig. 7 shows the source location process of the proposed algorithm and outputs some features of the middle layer of the network to show the mapping process of microseismic waveform transformation to the probability distribution image of the source location. In the coding network, after the microseismic data are input to the first layer, the height and width of the feature map are consistent with the input features, and the number of channels becomes 32. Then, in each downsampling operation, the width and height of the feature map are

halved, and the feature channels are doubled. The network model reduces the feature dimension through convolution and pooling operations; the final output features of the coding network are transmitted to the spatial hole multiscale pooling module, and the features after information mining and multiplexing are transmitted to the decoding network. The attention module further highlights the effective features in the upsampling process by feature weighting. The deconvolution operation restores the low-resolution source mapping map layer by layer to a high-resolution source location probability distribution image with the same spatial size as the input data space. Finally, the network learns the mapping relationship between the microseismic waveform and the source location, and the trained network can be used to predict the microseismic source location that is not involved in the training process.

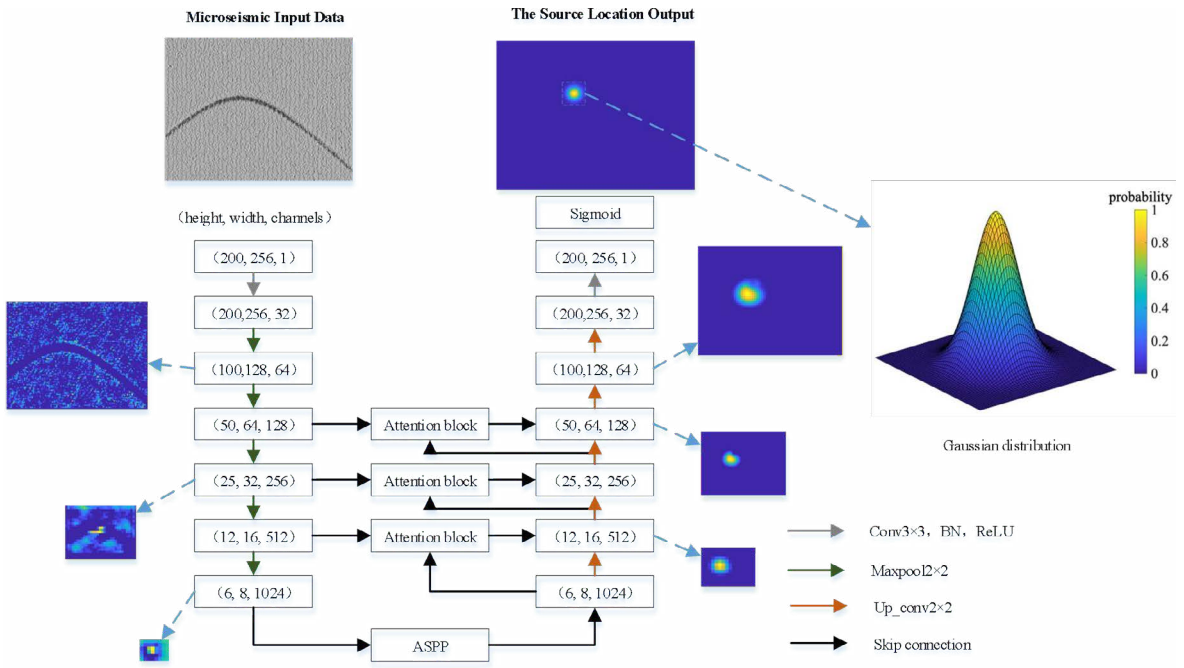


Fig. 7 Schematic diagram of network training process

The mean square error loss function is used to measure the difference between the predicted and actual source locations. The specific loss function expression is given by (4)

$$L = \frac{1}{N} \sum_{i=1}^N (l_i - \hat{l}_i)^2 \quad (4)$$

where  $N$  represents the total number of training samples,  $l_i$  denotes the source location information of the  $i$ th microseismic data predicted by the network, and  $\hat{l}_i$  denotes the corresponding true source location label. The smaller the loss function, the closer the network output is to the feature of the sample label and the higher the positioning accuracy.

The Adam optimizer is used to update the network, and the network performs 400 iterations. The initial learning rate of the training model is 0.01, and the batch size is set to 64. When the performance of the validation set is not improved after four iterations, the learning rate is automatically adjusted to half of the original.

The graphics processing unit used in the experiment is a GeForce RTX-3080 TI. The software platform uses Python3.8 environment. The network model is built using the PyTorch 1.6 framework. The CUDA version is 11.0.

## MODEL EXPERIMENT

### Simple layered velocity model

To verify the effectiveness of the proposed algorithm, a simple underground medium velocity model is developed, as shown in Fig.8. There are 256 grid points in the horizontal direction and 200 grid points in the vertical direction. The grid size is  $5\text{ m} \times 5\text{ m}$ . The velocity increases linearly with a change in depth, and the velocity range is 2–3 km/s. The geophone is arranged on the surface, and a geophone is set for each grid point in the horizontal direction. The sampling interval is 0.25 ms, and the monitoring time is 1800 ms.

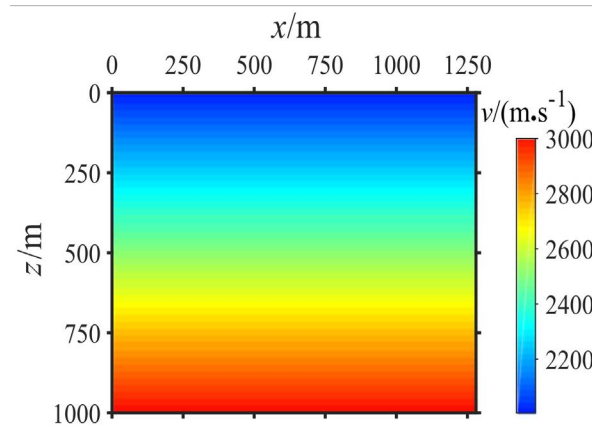


**Fig. 8** Simple layered velocity model

Single-shot data-related experiments: Several preprocessed single-shot datasets without noise and their corresponding source location labels are input into the network model for training, and the network performs 400 iterations. To test the fitting effect of the model more intuitively in the training process, the evaluation index error is set. The error is defined as the distance between the position of the maximum value in the network output feature and that in the sample label. Changes in the network loss and evaluation index with iteration rounds in the training process are shown in Fig.9. As the number of iterations increases, the network loss gradually decreases to convergence, and the error value gradually tends to 0, which proves that the output feature is very similar to the sample label and that the network feature fitting effect is improved.

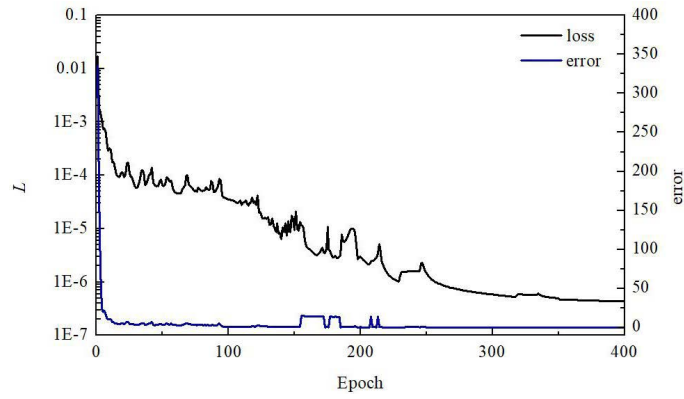
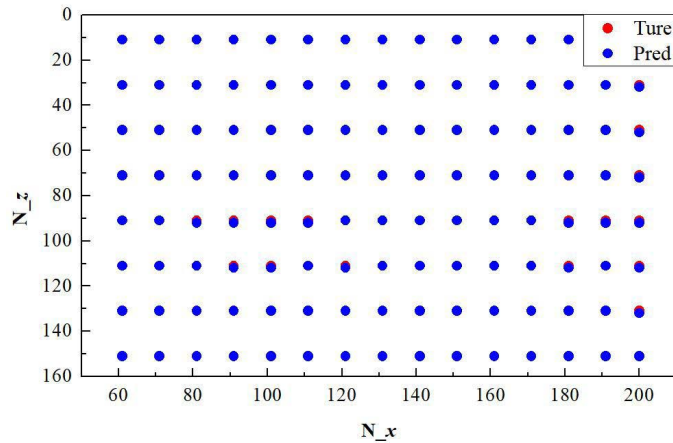


**Fig. 9** Curve of network performance with iteration rounds

The source is excited at the grid point to generate 120 test data points, which are transmitted to the trained network for source localization. Fig.10 shows the predicted source coordinates of the network and the actual source position. The red dots represent the actual source position, and the blue dots represent the predicted position of the network. The position predicted by the network is almost completely coincident with the actual position, and the maximum error in the x and z directions does not exceed 1 grid point.

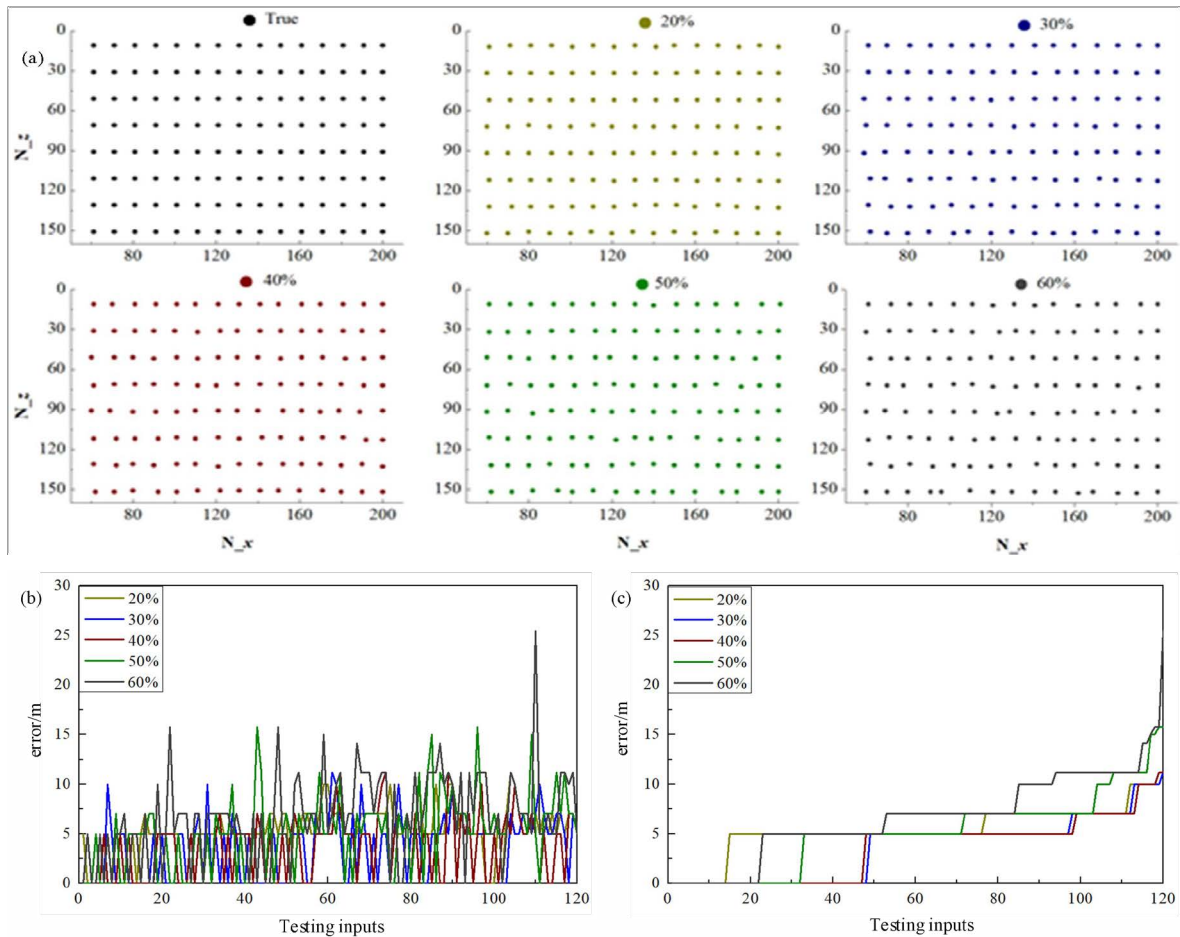


$N_x$  is the number of grid points in x direction,  $N_z$  is the number of grid points in z direction

**Fig. 10** Single shot data prediction results

The obtained microseismic data are introduced into the neural network for training after adding 20%–60% Gaussian random noise. Due to the multiplication of training data, the number of network iterations is reduced to 200. Different levels of noise are also added to the test dataset to test network performance, and the error between the predicted and actual coordinates of each microseismic data is calculated. The experimental results are shown in Fig.11. When the noise intensity is between 20% and 40%, network performance is improved. The predicted coordinates are almost distributed on the grid points and are close to the actual position. The maximum error in the 120 test data points is approximately 11.2 m (the error in the x direction is 1 grid point, and the error in the z direction is 2 grid points), and the prediction error of most

events is within 10 m. When the noise intensity is 50%–60%, the proportion of events with significant errors increases. Relevant positioning experiments of multiple sources are conducted: In this section, the slender fracture morphology is simulated, and 3–4 sources are used to describe the fracture morphology. The first source is randomly excited in the monitoring area, and the remaining sources are excited one by one along the set fracture morphology. The labels generated by each source are superimposed and normalized to represent the sample labels when multiple sources are used. The microseismic data of multiple shots and their corresponding labels are input into the neural network for training. Fig.12 shows the source position predicted by the trained network on the test data, and most of the predicted positions are completely coincident with the actual positions. The number of grid points ( $x_0, z_0$ ) is used to represent the source location at the  $x_0$  grid point in the x direction and  $z_0$  the grid point in the z direction.



(a) Location results under different levels of noise, (b) The positioning error of each test sample, (c) The result of plotting the error curve from small to large

**Fig. 11** Prediction Results and Errors under Different Noises

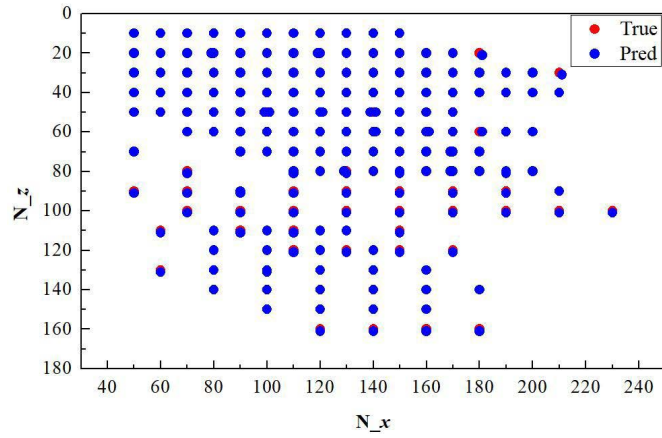
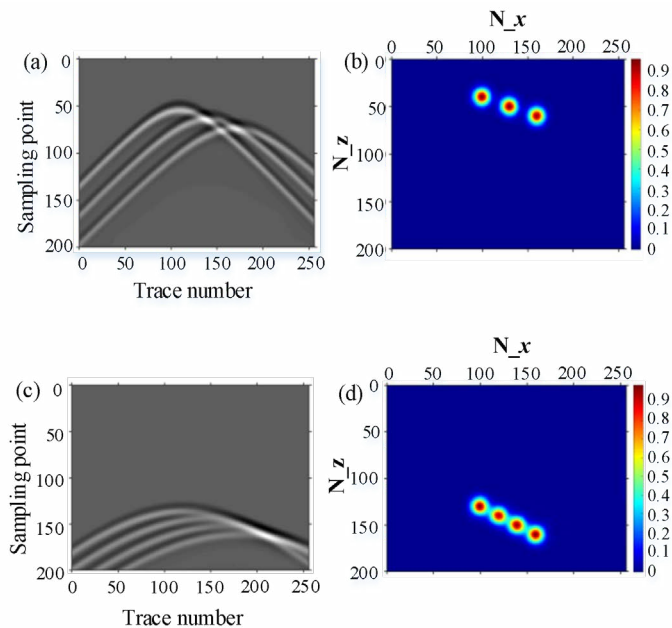


**Fig. 12** Prediction results of multi shot data

Fig.13a shows a test sample in the case of three sources. Fig.13b shows the corresponding positioning results. The three source positions predicted by the model are (100,40), (130,50), and (161,60), respectively. The prediction probabilities are 0.9534, 0.9616, and 0.9348, respectively. The prediction error of the third source is a grid point in the x direction, and the other two sources are accurate. Fig.13c shows a test sample with four seismic sources. Fig.13d shows the corresponding test results. The source locations predicted by the model are (130,100), (120,140), (140,150), and (160,161) grid points, respectively. The maximum error is one grid point, and the prediction probabilities are 0.9883, 0.9349, 0.9687, and 0.9893, respectively. For each source location of multishot data, the proposed algorithm can describe the real source point with a high probability of Gaussian distribution.



(a) Any test sample for three seismic sources; (b) The positioning results of the data in (a) figure; (c) Any test sample from four seismic sources; (d) The positioning results of the data in (c) figure.

**Fig. 13** Multiple shot test samples and positioning results

## Ablation experiment

Ablation experiments are conducted to verify the effectiveness of the proposed algorithm. To ensure the objectivity of the results, the training environment and hyperparameters of the different algorithms used in the comparative experiment are the same.

### 1) Analysis of the effect of cross-layer splicing structure:

The traditional U-Net algorithm is denoted as algorithm I, and the algorithm that only uses cross-layer splicing between deeper encoders and decoders is denoted as algorithm II. The two algorithms are trained on the noise-free single-source microseismic dataset. Changes in the network loss of the two algorithms with iteration rounds are shown in Fig.14. As the number of iterations increases, the network loss rapidly decreases. The network loss of algorithm II is less than that of algorithm I when the algorithm converges.

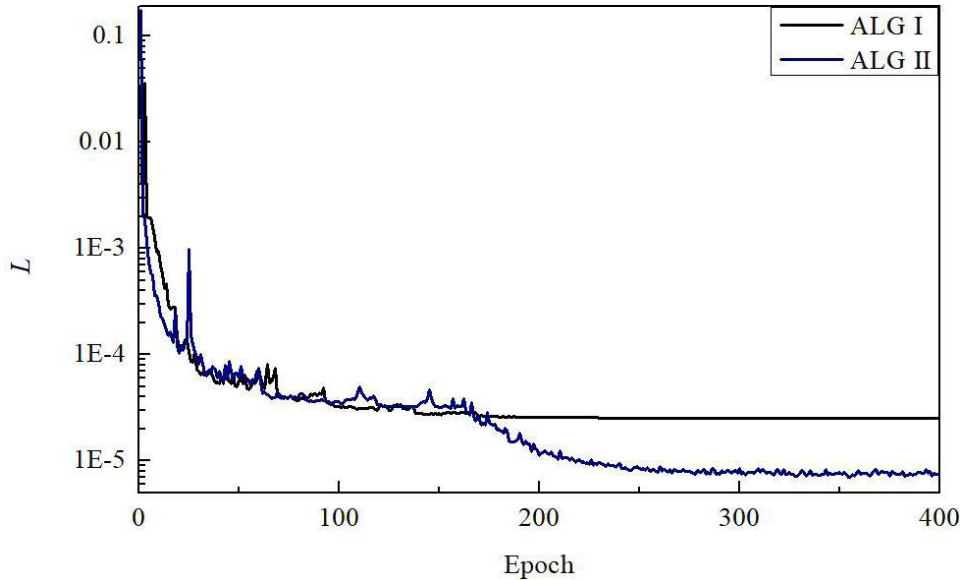
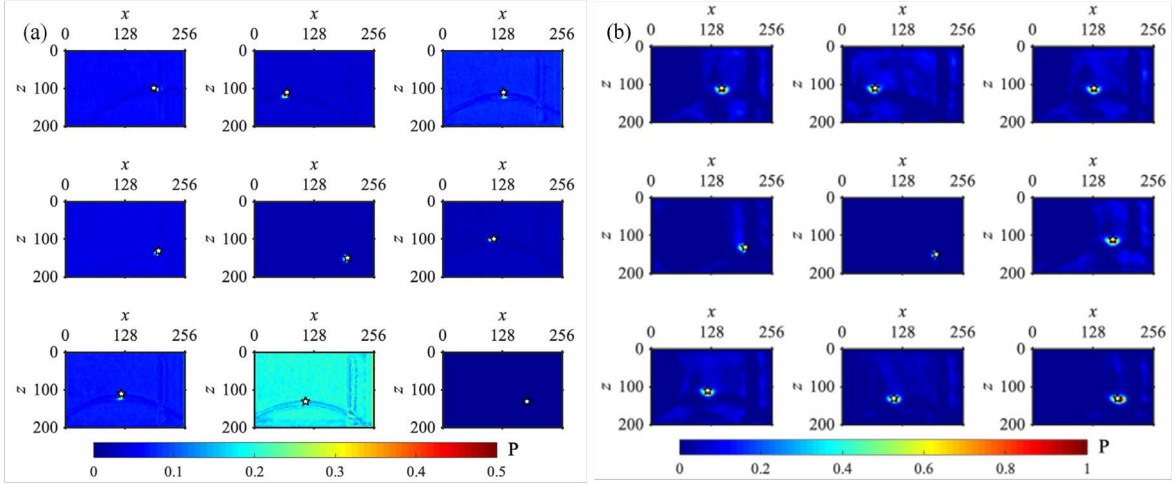


**Fig. 14** Comparison of Network Losses between Algorithm I and Algorithm II. ALG representation algorithm.

The antinoise performance of the two algorithms is observed when 10% noise disturbance is introduced into the test data. The test results are shown in Fig.15, where the yellow pentagram represents the actual source location. The figure shows that the probability value of the source position in the prediction results of algorithm I is low, and there are waveform artifacts in the figure that significantly influence the positioning result. The proportion of artifacts in the predicted output of algorithm II is low, and its predicted output is closer to the probability of the source location distribution.



(a) Is the corresponding result of Algorithm I; (b) Corresponding results for Algorithm II.

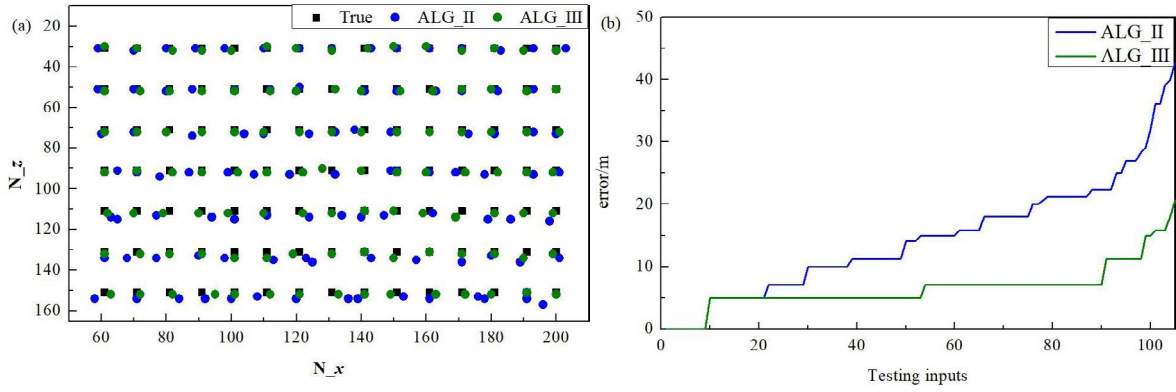
**Fig. 15** Partial Test Results of Algorithm I and Algorithm II for 10% Noise

The features extracted by the shallow encoder are biased toward texture detail information. In the positioning algorithm, the network learns the mapping from time-domain features to spatial-domain features. Algorithm I introduces detailed information about microseismic signals through cross-layer splicing into the high-level semantic features obtained using the deeper decoder, which negatively affects the positioning task. Algorithm II does not perform cross-layer splicing in the first two layers of the encoder–decoder structure, eliminates the interference of detailed features, and simplifies the network model to a certain extent.

Comprehensive analysis shows that algorithm II outperforms algorithm I. Under certain noise interference, the network using cross-layer splicing only between deeper codecs can accurately predict the location of the source, and the algorithm exhibits good robustness.

#### 1) Analysis of the role of the attention mechanism module:

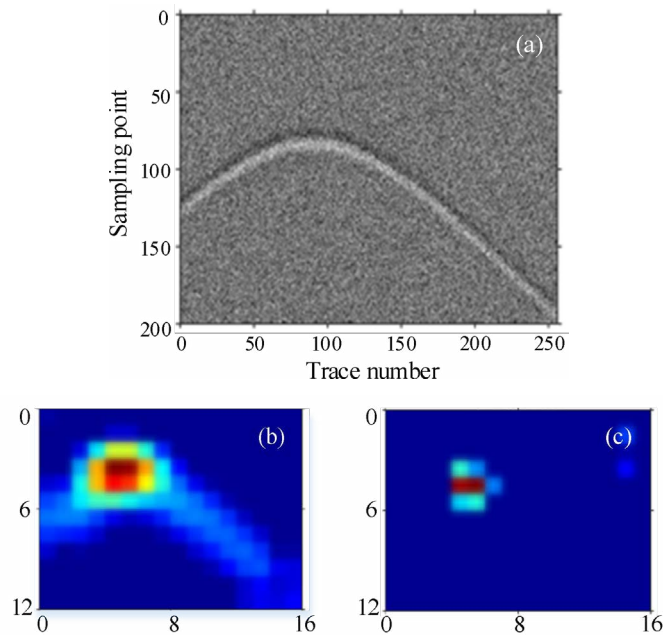
The function of the attention mechanism module is analyzed for high noise levels. The attention mechanism module is added to the network architecture of algorithm II, which is denoted as algorithm III. Using algorithms II and III to train the data after adding 50% random noise and using the data containing 50% noise for testing, the test results and positioning error are shown in Fig.16, where the black dot represents the actual source position, and the blue and green dots represent the predicted position coordinates of algorithms II and III, respectively. The test errors are arranged from small to large to obtain the line chart shown in Fig.16b. The prediction results of algorithm III are closer to the actual position coordinates, and the error is smaller.



(a) Test results of Algorithm II and Algorithm III; (b) The result of plotting the error curves of Algorithm II and Algorithm III from small to large

**Fig. 16** Test results and errors of Algorithm II and Algorithm III

Select any noisy data in the test sample, as shown in Fig.17a, with its true coordinates located at grid points (90, 70). Use algorithms II and III to test the data and visualize the extracted feature maps. The features of the two algorithms in the last layer of the encoder are shown in Fig.17b and 17c. Feature map analysis reveals that algorithm II still has the original waveform information in the features of the last layer of the encoder; there is incomplete fitting of the source position information. The attention mechanism in algorithm III can focus the network on feature extraction of position information during the encoding process of microseismic data, thereby reducing irrelevant noise and waveform interference.

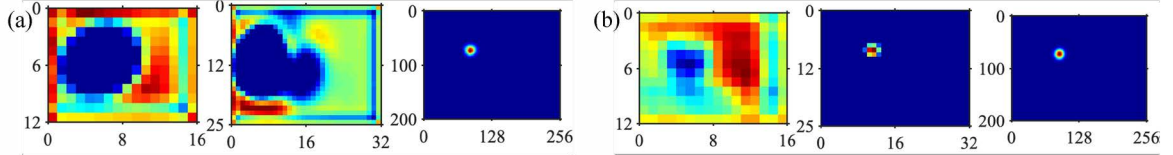


(a) Display of any noisy test sample; (b) Features in the last layer encoder of Algorithm II; (c) Features in the last layer encoder in Algorithm III

**Fig. 17** Any noisy test data and features in the last layer encoder

Some features in the decoder are shown in Fig.18. The decoding network extracts the feature set that is more important to the positioning task in the lower layer and the same level in the coding

network through a weighted form of the attention coefficient, excludes the influence of nonmain factors, and locates the source position. For the prediction of the source location, algorithm II predicts that the source is located at (87,73) grid points, and algorithm III, incorporating an attention mechanism, predicts that the coordinates are (90,71), which is closer to the actual source location.



(a) Features in the first, second-, and fifth-layer decoders of Algorithm II; (b) Features in Layer 1, Layer 2, and Layer 5 decoders in Algorithm III

**Fig. 18** Partial Features in Algorithm II and Algorithm III Decoders

Comprehensive analysis shows that algorithm III outperforms algorithm II. The incorporation of an attention mechanism can help the model accurately focus on the source position under strong noise interference, which is more suitable for the case of low SNR of microseismic signals.

## 2) Analysis of the role of the ASPP module:

Analyze the role of spatial voids and multiscale pooling modules for multiple sources. Add an ASPP module to the network architecture of algorithm III, namely, the algorithm MEL-Net proposed in this study. The network losses of the two algorithms on the validation set are shown in Fig.19, indicating that the MEL-Net model has better learning and mapping capabilities than algorithm III. To further analyze the performance of the ASPP module, we visualize the features of the middle layer of the network. The features in the first three decoder layers are shown in Fig.20.

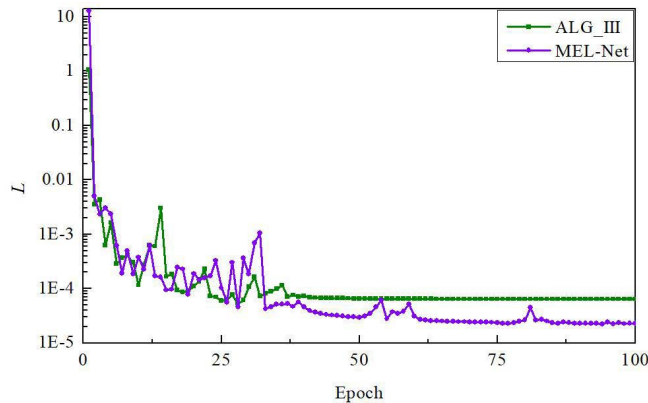


**Fig. 19** Comparison of Network Loss on Algorithm III and MEL-Net Verification Set

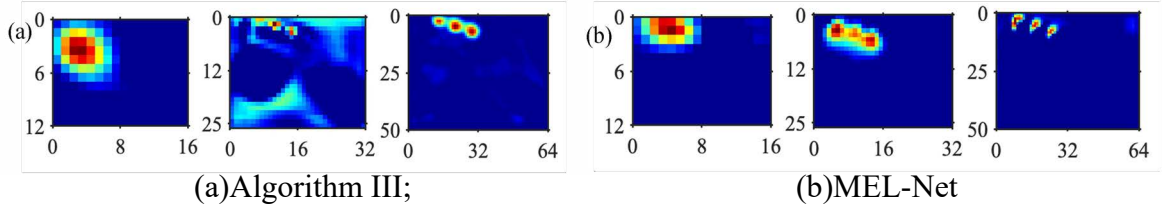


**Fig. 20** Algorithm III and features in the first three layers of MEL-Net decoders

In the coding process, the network is extracted from shallow pixel-level features to deep semantic-level features. In this study, the ASPP module is used between the underlying encoder–decoder structure of the network, and multiscale information fusion is performed using different scales of dilated convolutions. The deep feature information extracted by the last layer of the encoder is deeply mined so that the information obtained by the decoder becomes more focused. In the process of layer-by-layer decoding of the network, more stable feature extraction is performed, and an accurate source location is obtained.

Comprehensive analysis shows that MEL-Net outperforms algorithm III. With the incorporation of the space hole multiscale pooling module, high-level semantic information can be deeply mined to realize precise positioning operations in the case of multiple sources.

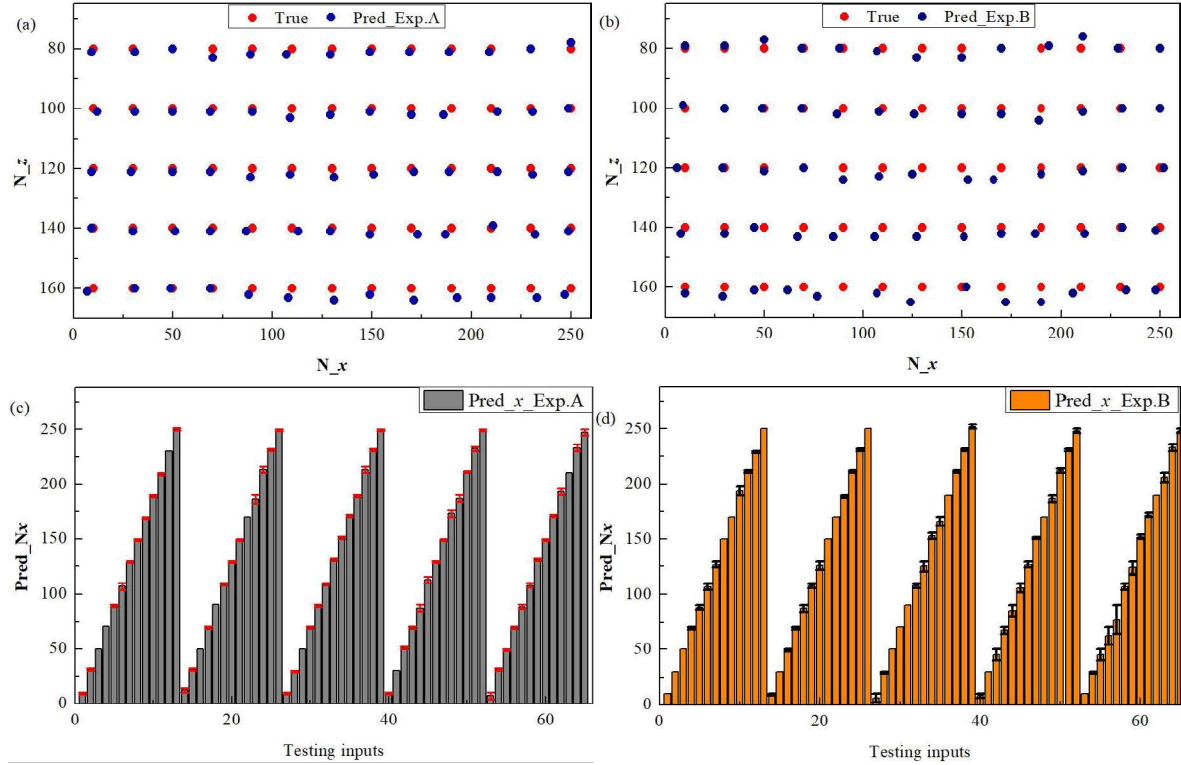
Based on the results of the above ablation experiments, different algorithm models are analyzed from the perspectives of positioning effect, positioning error, network loss, and intermediate layer characteristics. The network performance of the improved model is enhanced to varying degrees. The experimental results show that the proposed algorithm outperforms the other algorithms, which confirms its effectiveness. Complicated marmousi velocity model

The Marmousi speed model is selected to verify the positioning ability of the proposed algorithm under a complex speed model. There are 288 grid points in the horizontal direction and 300 grid points in the vertical direction. The grid spacing is 8 m. Among them, 288 geophones are equidistantly arranged along the surface, and the channel spacing is 8 m. The sampling time interval is 0.3 ms, and the recording length is 2700 ms.

Experiments using smoothing operators with sizes of  $4 \times 4$  and  $6 \times 6$  are recorded as

Experiments A and B, respectively. The microseismic data generated by different smoothness models are trained by the network. After the training is completed, the test dataset constructed using the actual velocity model is used for testing. There are 65 test data points. Fig.21 shows the positioning results on the test data from the two experiments and the error bar chart in the x and z directions. The red dots represent the actual source position, and the dark blue dots represent the network prediction position. The abscissa of the error bar

graph represents the number of test data points, and the ordinate represents the coordinates in the x and z directions predicted by the network. The short red line in the graph represents the error line predicted by Experiment A for the coordinate position, and the short black line represents the error line predicted by Experiment B for the coordinate position. The figure shows that when the velocity model is accurate, the positioning accuracy improves. If the speed model deviation is severe, the feature difference between the training and test datasets is significant, and there is a certain error in the positioning effect.



(a) And (b) are the positioning results of Experiment A and Experiment B, respectively, Pred\_Exp. A represents the predicted result of Experiment A, Pred\_Exp. B represents the predicted result of Experiment B; (c) And (d) are the positioning coordinates and errors of the two experiments in the x-direction, Pred\_Nx represents the predicted result in the x direction, Pred\_X\_Exp. A represents the prediction of experiment A for the x-coordinate, Pred\_X\_Exp. B represents the prediction of the x coordinate in Experiment B; (e) And (f) are the positioning coordinates and errors of the two experiments in the z-direction, Pred\_Nz represents the predicted result in the z-direction,

Pred\_Z\_Exp. A represents the prediction of Experiment A for the z-coordinate, Pred\_Z\_Exp. B represents the prediction of z coordinate in Experiment B

**Fig. 21** Test results and errors of Experiment A and Experiment B

The sensitivity of the network to noise is tested. Taking the training data generated by the smoothing model as an example, after randomly adding 20%–60% Gaussian noise, the network is trained. The number of network iterations is 200, which is recorded as Experiment C. After adding different levels of noise

to the test dataset, the experiment is conducted. The noisy data with different levels of noise added to the same data are shown in Fig.22. When the noise level intensity is not high, the effective waveform of the microseismic data can be distinguished. As the noise intensity increases, the waveform information is gradually submerged by the noise signal.

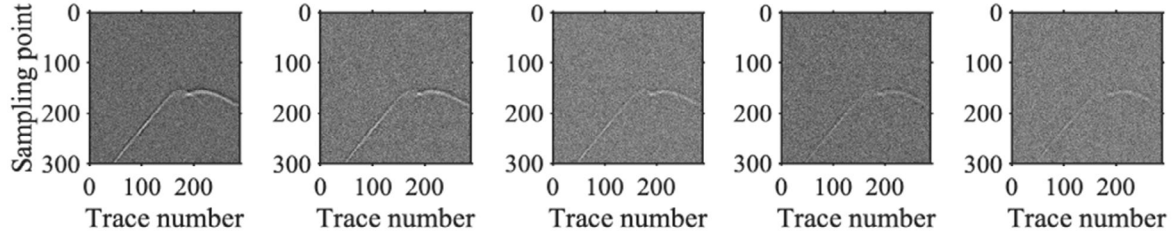


**Fig. 22** The results of adding different levels of noise to the same data

Fig.23 shows the network performance under different noise levels. From the analysis of the positioning results, the algorithm has better antinoise performance and higher accuracy when the noise intensity is low. When the noise intensity is strong, and the effective signal cannot be distinguished, the positioning accuracy is affected to a certain extent; however, the degree of position deviation is small, and the positioning result is still close to the actual position. In summary, the MEL-Net network can maintain high positioning accuracy for low-SNR microseismic data with velocity errors under complex geological conditions.

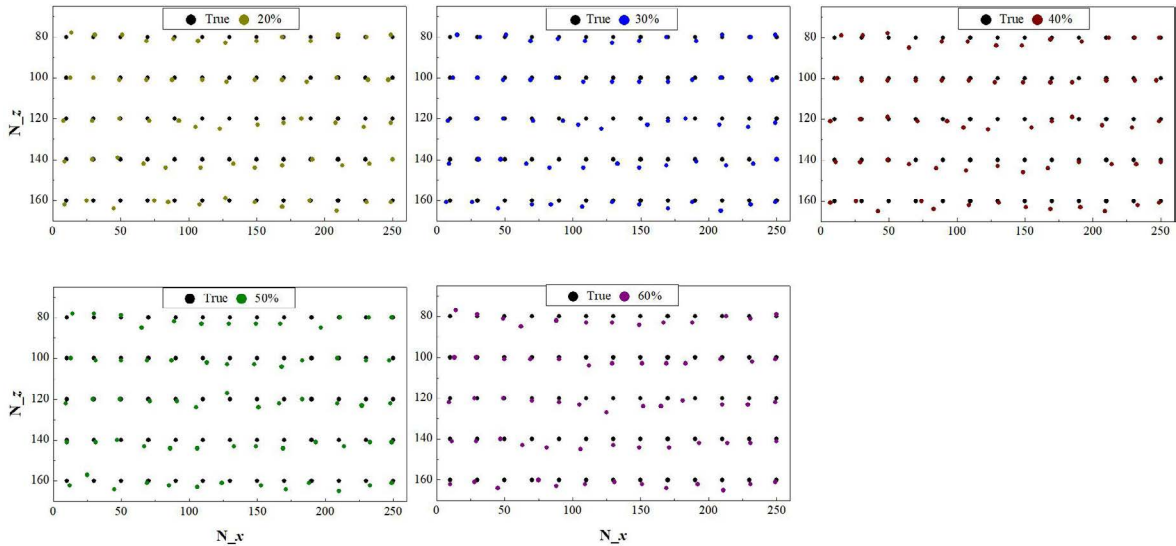


**Fig. 23** Prediction results under different noises

### Comparison with the traditional reverse-time positioning method

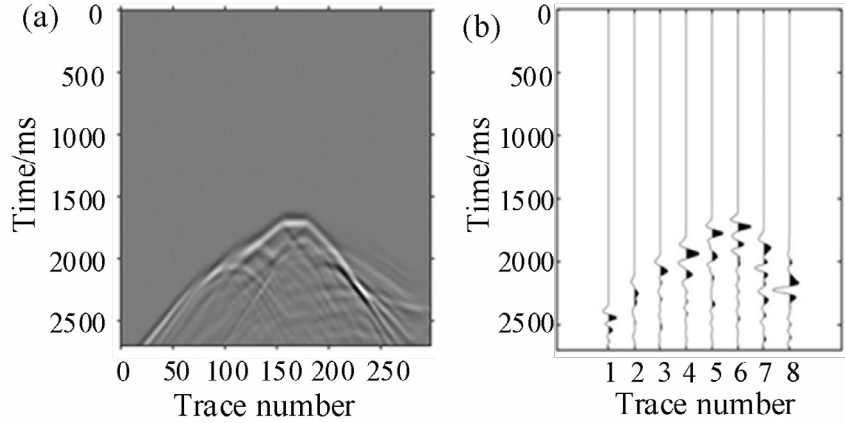
The microseismic reverse-time positioning method takes microseismic data received by geophones as input data and regards the geophone position as a

new source point position to reverse-time extend the wave field. According to the principle of time consistency, a suitable imaging method is used to describe the source position. In the comparison experiment described in this section, the cross-correlation imaging condition is selected, and the grid point with the highest imaging value is the source. The mathematical expression of the cross-correlation imaging method is as follows:

$$\text{Image}(x, z) = \sum_t^{t_{\max}} s(x, z, t) \cdot r(x, z, t) \quad (5)$$

where  $s(x, z, t)$  denotes the source wave field,  $r(x, z, t)$  denotes the detector wave field, and  $\text{Image}(x, z)$  denotes the cross-correlation operation of the source and detector wave fields at time  $t$ . The cross-correlation wave field is superimposed along the time dimension to obtain the imaging result.

To evaluate the influence of velocity model errors on the positioning accuracy of reverse-time imaging, the smoothed velocity model is used as the initial model, and the reverse-time wave field is reversed using the microseismic record generated by the actual velocity model. Fig.24a shows the synthetic record profile excited by the source position at the (170, 140) grid point. Eight geophone records (Fig.24b) are selected for the experiment.

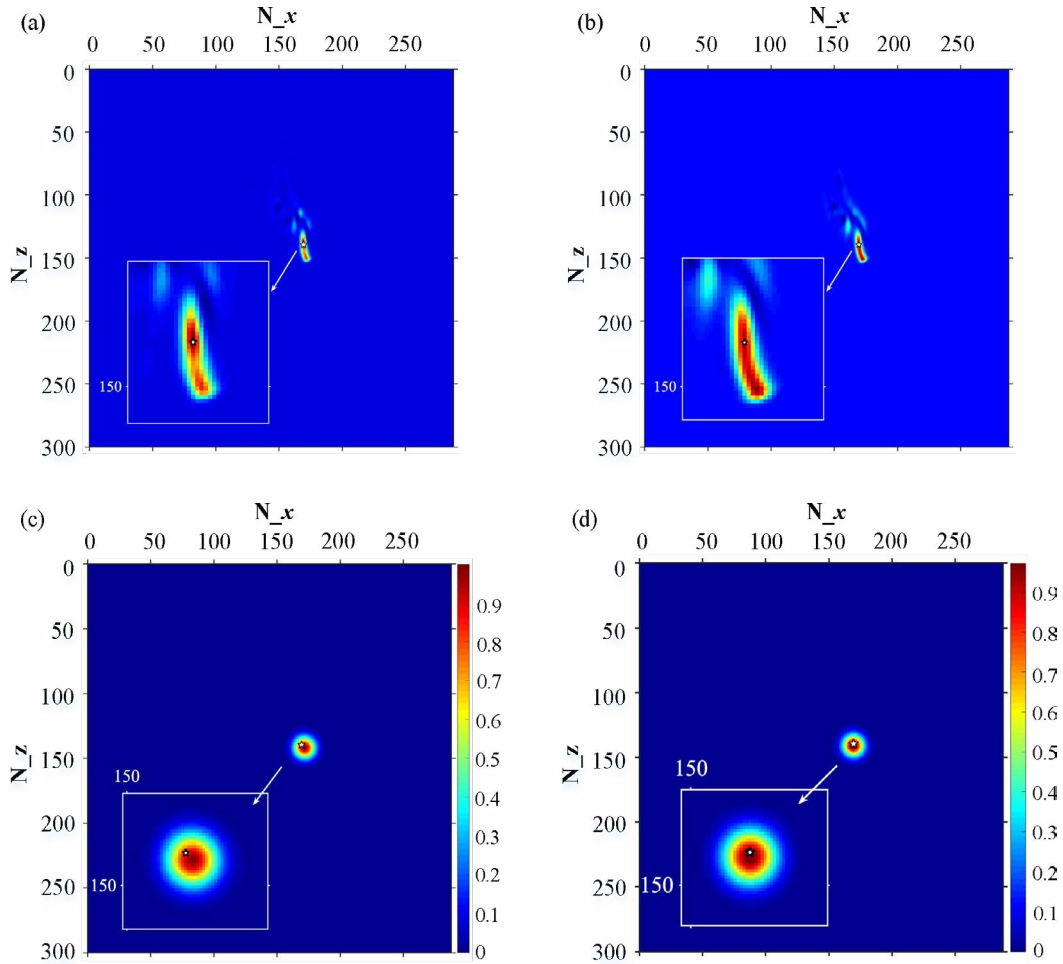


(a) Data accepted by all geophones, (b) Data accepted by the 8 selected geophones

Fig. 24: The microseismic data

Reverse-time positioning experiments were conducted on velocity models with smoothing factors of  $4 \times 4$  and  $6 \times 6$ , which are denoted as Experiments D and E, respectively. Fig.25a and

Fig.25b show the positioning effect diagrams obtained from Experiments D and E, respectively. The microseismic record is introduced into Experiments A and B obtained from the MEL-Net model training for testing. The test results are shown in Fig.25c and 25d. The white pentagram represents the actual source position, and the lower left corner shows an enlarged display of the imaging results.



(a) And (b) are the results obtained from the inverse time localization algorithm, corresponding to Experiment D and Experiment E respectively; (c) (d) represents the results obtained from the MEL-Net model, corresponding to Experiment A and Experiment B, respectively

**Fig. 25** Comparison of localization results between inverse time localization algorithm and deep learning algorithm From the experimental results, the reverse-time location algorithm has a more obvious energy group at the actual source location, and the location of the maximum energy in the energy group is

the inverse source location. The source location coordinates obtained by Experiment D are (170, 139), and the maximum imaging value of Experiment E is (173, 151). When the velocity model error is small, the energy focusing of the positioning algorithm is strong. When the accuracy of the velocity model is low, the energy is dispersed, significantly affecting the positioning accuracy. Experiment A predicted the source position to be (172,142), with a prediction probability of 0.9879. The prediction results of Experiment B were obtained at grid points (170,142). In contrast, the positioning results obtained by the CNN MEL-Net exhibited stable imaging performance under different velocity model errors, and the resolution of the imaging position was unaffected by velocity model errors, resulting in higher positioning accuracy.

The number of geophones typically determines the accuracy of imaging. A full detection point record is selected, as shown in Fig.26. Reverse-time imaging under different observation systems is performed without velocity model errors, and the positioning accuracy and time consumption are compared. Four groups of different numbers of observation systems are selected. The first group involves 5 geophones with an interval of 560 m. The second group consists of 8 detectors with an interval of 320 m. The third group consists of 15 detectors with an interval of 160 m. The fourth group involves 20 geophones with an interval of 120 m. The microseismic signals received are shown in Fig.27.

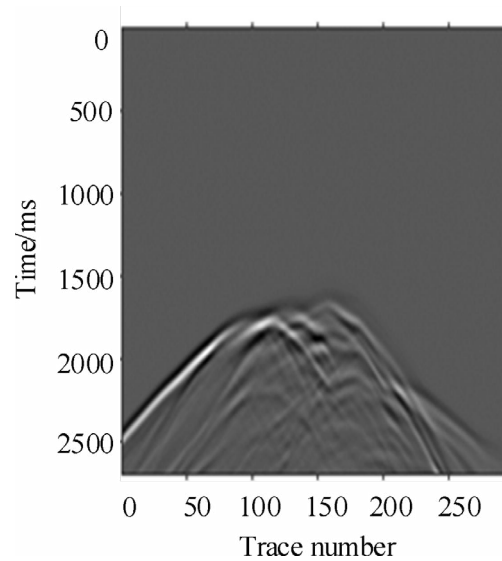
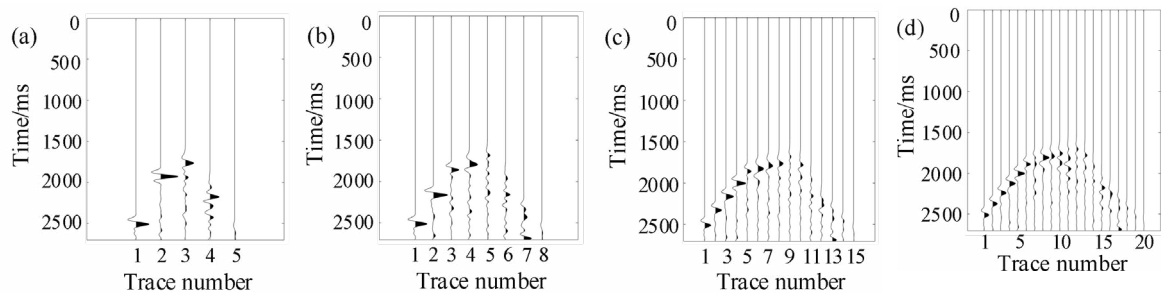


**Fig. 26** The microseismic data

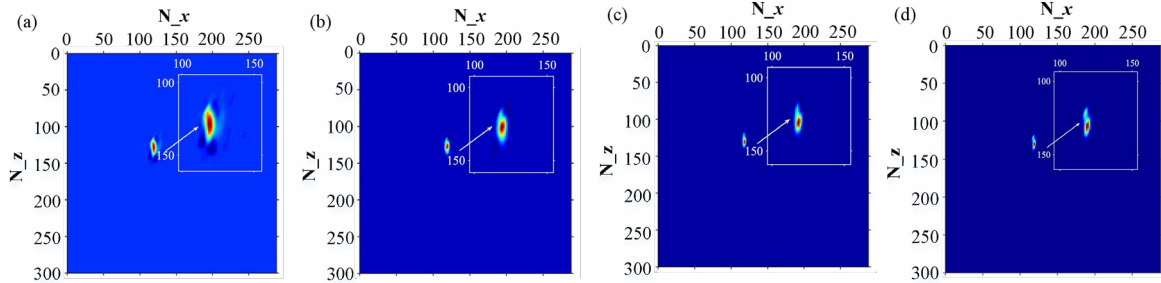


(a), (b), (c), and (d) correspond to the microseismic signals received by the first to fourth observation systems, respectively.

**Fig. 27** Microseismic records obtained from different observation systems

With the  $6 \times 6$  operator smoothed model as the migration velocity model, the cross-correlation imaging conditions are used to image the source. The imaging results are shown in Fig.28, and the upper right corner shows the magnification of the imaging. Fig.29 shows the calculation time and positioning error for each observation system. As the number of geophones increases, the positioning effect on illusion suppression, the resolution at the source position, and positioning

accuracy improve. However, this method performs independent operations on the reverse wave field of the detector during imaging. The increase in the number of detectors makes the corresponding operation process more complicated and significantly increases the calculation time. It is difficult to meet the needs of real-time positioning in practical engineering applications.



(a), (b), (c), and (d) correspond to the positioning results of the first to fourth observation systems, respectively.

**Fig. 28** Imaging results of different observation systems

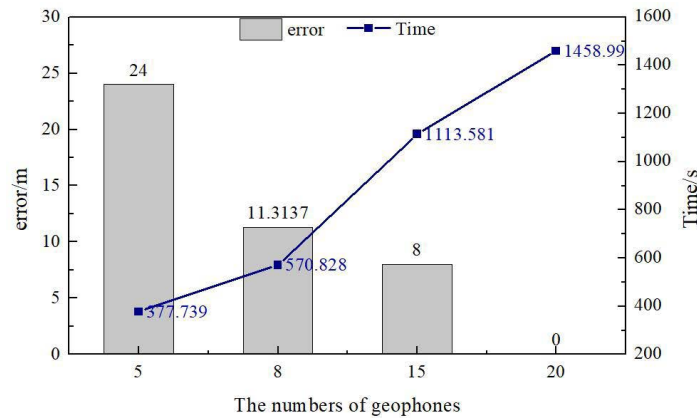
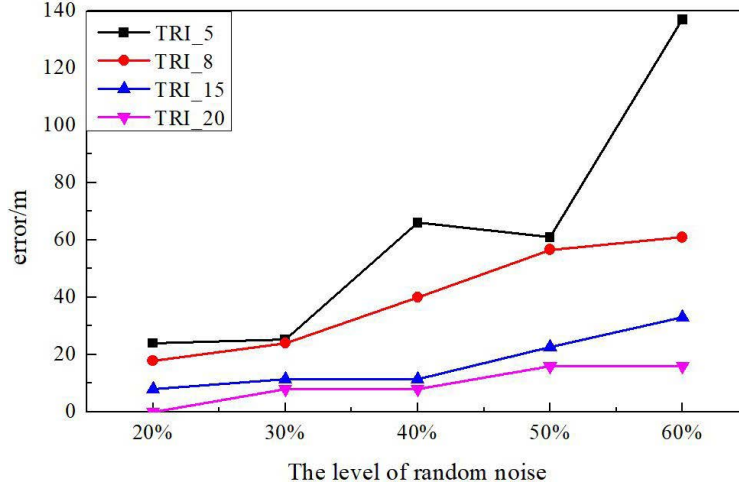


**Fig. 29** Calculation time and positioning error of different observation systems

An antinoise experiment using the traditional reverse-time positioning algorithm is conducted. Different levels of random noise are added to the synthetic record obtained from Fig.26, and the noisy wave field record is back-transmitted to the initial velocity model obtained by the  $4 \times 4$  smoothing operator. The positioning errors of the traditional algorithm for the four sets of observation systems are shown in Fig.30.

The statistical results show that the reverse-time positioning algorithm exhibits antinoise performance and is more robust at low noise levels. However, when there is strong random noise in the microseismic record, the method requires more detectors to suppress the noise, which means that source positioning takes a long time. If the number of detection points selected is insufficient, noise interference reduces the correlation between microseismic signal channels and channels, and the energy cannot be accurately focused, resulting in positioning

errors. In the case of low SNRs, it is difficult for the reverse-time positioning algorithm to effectively focus the energy on the actual source position when the wave field is reversed, which degrades the positioning accuracy.



TRI\_ Indicates the experiment using the inverse time positioning algorithm, and the number received is the number of detectors used

**Fig. 30** The positioning error of inverse time localization algorithm under different noise conditions

Based on the data-driven principle of deep learning, MEL-Net considers the influence of noise when constructing dataset samples. Therefore, the imaging effect is stable during the test process, and it has a more robust positioning process for noise interference with different intensities than the traditional reverse-time positioning algorithm. Due to the characteristics of CNNs, MEL-Net has an “end-to-end” processing mode and can directly use the pretrained model to predict unknown samples. The calculation time corresponding to the positioning results shown in Fig.23 is calculated. For noisy data, the average positioning time of MEL-Net is  $1.22 \times 10^{-4}$  s. Compared with the inverse-time positioning algorithm, it can significantly improve positioning efficiency while ensuring positioning accuracy and completing the positioning task at a lower computational cost.

## DISCUSSION AND CONCLUSIONS

In this study, a neural network structure, MEL-Net, that integrates an attention mechanism and the multiscale pooling module of the spatial cavity is proposed to directly predict the location of the corresponding event source according to the waveform characteristics of microseismic signals. In contrast to other positioning algorithms, the influence of noise interference and velocity model errors on source positioning accuracy is considered in the proposed algorithm. The attention mechanism and ASPP module are introduced to improve the feature extraction ability of the network. Through model experiments in simple and complex velocity media, the following conclusions are drawn:

1) The proposed CNN MEL-Net can extract features from microseismic waveform data and map them to the 2D Gaussian distribution of the source location with high accuracy. The attention mechanism module is used to guide the network in extracting relevant waveform information under background noise interference through weight distribution. The ASPP module is used to expand the receptive field in the network learning process, and multiscale feature extraction is performed on the final high-level information obtained using the coding network. To solve the problem of weak correspondence in the element space in the mapping process, the effects of shallow information on the positioning task are eliminated by only performing cross-layer splicing at the deeper level. Comparing the proposed algorithm with similar algorithms through ablation experiments, it has superior antinoise performance and positioning accuracy.

2) Deep learning is data-driven, and the performance of the network model depends, to a certain extent, on the construction of the sample dataset. In this study, large-scale microseismic datasets are constructed by forward calculations of a given velocity model. The input and output dimensions of the network are the same by uniformly downsampling the time-series dimension of microseismic signals. The feature dimension is reduced while the position information of the waveform is retained. To solve the problem of low SNR of microseismic data and the influence of many factors on source positioning accuracy, the original velocity model is smoothed to introduce velocity model errors, and different intensities of Gaussian noise are added for simulations. In the test process, on the microseismic data with low SNRs and velocity model errors, the positioning accuracy of the MEL-Net network does not decrease significantly, and the obtained model exhibits strong robustness and generalization.

3) In terms of the positioning effect, after the network training is completed, the proposed algorithm, taking the microseismic waveform not used in the training as the input, can predict the corresponding source position in milliseconds. This process does not require manual intervention and realizes intelligent and automatic source positioning using microseismic data. Compared with the reverse-time positioning algorithm, the positioning accuracy of the MEL-Net model is similar to that when using more detectors for reverse-time extension. The calculation cost and calculation time are significantly reduced, which alleviates the trade-off between positioning accuracy and positioning efficiency of traditional algorithms to a certain extent.

The premise of the application of the proposed algorithm is that microseismic events are detected. In practical applications, there may be a significant difference between the microseismic waveform and training data. The entry point of follow-up research is to apply prior knowledge obtained from the source domain to the target task in combination with the idea of transfer learning to solve the positioning problem of actual data. In addition, a CNN model is a “black box

model,” and another research direction is to improve the interpretability of the model by introducing geophysical knowledge into the network.

## ACKNOWLEDGMENTS

**Funding:** This work was supported by the National Natural Science Foundation of China under Grant U21A2019; Natural Science Foundation of Heilongjiang Province under Grant LH2023D009.

## REFERENCES

- Cheng Jiulong, Song Guangdong, Sun Xiaoyun, Wen Laifu, Li Fei. Research Developments and Prospects on Microseismic Source Location in Mines. *Engineering*, 2018,4(5):653-660.
- Chen L. -C., Papandreou G., Kokkinos I., Murphy K., Alan L. Yuille. DeepLab: Semantic Image Segmentation with Deep Convolutional Nets, Atrous Convolution, and Fully Connected CRFs. in *IEEE Transactions on Pattern Analysis and Machine Intelligence*, 2018,40(4):834-848.
- Cheng Qian, Wei Wei, Fu LiYun. Accuracy analysis of borehole observation microseismic location based on time reverse imaging. *Chinese Journal of Geophysics*, 2022,65(8): 3213-3228.
- F. Li, Y. Qin, W. Song, 2019. Waveform inversion-assisted distributed reverse time migration for microseismic location. in *IEEE Journal of Selected Topics in Applied Earth Observations and Remote Sensing*, 2019,12(4): 1327-1332.
- Feng Q., Pan B., Han L, Pan Zhang. Microseismic Source Location Estimation Using Reverse Double-Difference Time Imaging. in *IEEE Access*, 2021,9:66032-66042.
- FENG Qiang, PAN BaoZhi, HAN LiGuo. Microseismic source location method based on convolutional denoising auto-encoder and softmax regression. *Chinese Journal of Geophysics (in Chinese)*, 2023,66(7): 3076-3085.
- Ge Qixin, Han Liguu, Cai Zhongzheng, 2019. Reverse travel time imaging of microseismic location. *Exploration Geophysics*, 50:3, 281-296.
- Guo X B, Liu H, Shi Y. Modified interferometric imaging condition for reverse-time migration. *Exploration Geophysics*, 2018, 49(2): 202-212.
- Huang, L Q; Li, J; Hao, H; Li, XB. Micro-seismic event detection and location in underground mines by using Convolutional Neural Networks (CNN) and deep learning[J]. *TUNNELLING AND UNDERGROUND SPACE TECHNOLOGY*.2018,81(1):265-276.
- Li Meng, Li Huifeng, Guo Tao, Mohammed Ali b, Yuhua Guo c. Microseismic event location using multi-scale time reversed imaging. *Journal of Petroleum Science and Engineering*, 2019, 174: 144-160.
- Long J, Shelhamer E, Darrell T. Fully Convolutional Networks for Semantic Segmentation. *IEEE Transactions on Pattern Analysis and Machine Intelligence*, 2015,39(4):640-651.

- Ma K., Sun X., Zhang Z. Hu Jing, Wang Zuorong. Intelligent Location of Microseismic Events Based on a Fully Convolutional Neural Network (FCNN). *Rock Mechanics & Rock Engineering*, 2022,55(8):1-17.
- Paul Sava, 2011. Micro-earthquake monitoring with sparsely sampled data. *Journal of Petroleum Exploration&Production Technology*. 2011,1(1).43-49.
- Perol T, Gharbi M, Denolle M. Convolutional neural network for earthquake detection and location. *Science Advances*, 2018, 4(2): e1700578.
- Ronneberger O, Fischer P, Brox T. U-Net: Convolutional Networks for Biomedical Image Segmentation. Springer International Publishing, 2015:234-241.
- Saad O M, Bai M, Chen Y. Uncovering the microseismic signals from noisy data for high- fidelity 3D source-location imaging using deep learningMicroseismic denoising. *Geophysics*: 2021,86(6):161-173.
- TANG Jie, LIU YingChang, LI Cong, SUN ChengYu. Reverse time location of microseismic source and fracture imaging with attenuation compensation in viscoelastic medium based on low rank approximation. *Chinese Journal of Geophysics (in Chinese)*, 2021,64(8): 2858-2876.
- TIAN Xiao, ZHANG Xiong, ZHANG Hua, MA ChangYing, DAI MengXue, CHU FangDong. Full-interferometry imaging method for microseismic location. *Chinese Journal of Geophysics (in Chinese)*, 63(8): 3105-3115.
- Vinard, N. A., Drijkoningen, G. G., Verschuur, D. J., Dmitry Alexandrov, Leo Eisner. Localizing weak microseismic events using transfer learning with a deep neural network. *Geophysical Prospecting*, 2022,70(7), 1212-1227.
- Vinard N A, Drijkoningen G G, Verschuur D J, 2021. Localizing microseismic events on field data using a U-Net-based convolutional neural network trained on synthetic data. *Geophysics*, 2021, 87(2): KS33-KS43.
- WANG Jiachen, ZHANG Haijiang, ZHAO Lipeng, ZHA Huasheng, CHENG Tingting, SHI Xiaohong, QIAN Jiawei, LIU Ying, Michal Malinowski, LINGHU Jianshe. Evaluation of the coalbed methane hydraulic fracturing effect based on microseismic event locations and tomography results for surface microseismic monitoring. *Geophysical Prospecting for Petroleum*. 2023, 62(1): 31-42.
- WANG Chen-Long, CHENG Jiu-Bing, YIN Chen, LIU Hong. Microseismic events location of surface and borehole observation with reverse-time focusing using interferometry technique. *Chinese Journal of Geophysics (in Chinese)*, 2013, 56(9): 3184-3196.
- Wang H, Alkhalifah T A. Direct microseismic event location and characterization from passive seismic data using convolutional neural networks. *Society of Exploration Geophysicists*, 2021(6):109-121.
- Wamriew D, Charara M, Pissarenko D. Joint event location and velocity model update in real-time for downhole microseismic monitoring: A deep learning approach. *Computers & geosciences*, 2022(158):104965.

- XU Li-Sheng, DU Hai-Lin, YAN Chuan, LI Chun Lai. A method for determination of earthquake hypocentroid: time-reversal imaging technique I--Principle and numerical tests. *Chinese Journal of Geophysics*, 2013,56(4):1190-1206.
- Yuan Jianlong, Yu Jiashun, Fu Xiaobo, Han Chao. Antinoise performance of time-reverse imaging conditions for microseismic location. *Geophysics* 2020, 85 (3): KS75–KS87.
- Zhang Lingli, Ren Yuxiao, Chen Lei, Kai Wang, Xinji Xu, Xiaobin Xu, Chao Fu. A new denoising strategy and the X-shaped supplement denoising operator targeting time- reversed mirror imaging technique, *Journal of Geophysics and Engineering*, 2021,18(4):503–514.
- Zhang Xiong, Zhang Jie, Yuan Congcong, Liu Sen, Chen Zhibo, Li Weiping. Locating induced earthquakes with a network of seismic stations in Oklahoma via a deep learning method. *Scientific Reports*. 2020,10(1):1941.
- Zhang Xiong, Chen Huihui, Zhang Wei, Tian Xiao; Chu Fangdong. Generalized neural network trained with a small amount of base samples: Application to event detection and phase picking in downhole microseismic monitoring. *Geophysics* 2021, 86 (5): KS95–KS108.
- Zhang, Y., Liu, X.Q., Song, L.W. and Dong, H.L. Microseismic event detection based on multiscale detection convolutional neural network[J]. *Journal of Seismic Exploration*, 2023,32(5): 455-477.
- Zhang Y., Meng D., Zhou Y., Song L., and Dong H. Seismic Velocity Inversion Based on Physically Constrained Neural Networks[J]. *IEEE Transactions on Geoscience and Remote Sensing*, 2024,62:5900717-1-17.